

ENGINEERING

Non–von Neumann multi-input spike signal processing enabled by an artificial synaptic multiplexer

Dong Hae Ho^{1†}, Dong Gue Roe^{2†}, Yoon Young Choi³, Seongchan Kim⁴, Young Jin Choi¹, Do Hwan Kim⁵, Sae Byeok Jo¹, Jeong Ho Cho^{1*}

Multiplexing is essential for technologies that require processing of a large amount of information in real time. Here, we present an artificial synaptic multiplexing unit capable of realizing parallel multi-input control system. Ion gel was used as a dielectric layer of the artificial synaptic multiplexing unit because of its ionic property, allowing multigating for parallel input. A closed-loop control system that enables multi-input–based feedback for actuator bending control was realized by incorporating an ion gel–based artificial synaptic multiplexing unit, an actuator, and a bending angle sensor. The proposed multi-input control system could simultaneously process input and feedback signals, offering a breakthrough in industries in which the processing of vast amounts of streaming data is essential.

INTRODUCTION

The importance of the ability to collect information about the surrounding environment is growing in various related fields, such as health care, autonomous vehicles, and smart manufacturing, as it is essential for artificial intelligence (AI) devices to make decisions (1–4). Information on the surrounding environment is obtained using sensor networks, and thus, the amount of obtainable information is determined by the number of sensors in the network (4). This implies that the active and preemptive response of AI devices relies on the densification of the sensor network (5–11), which inevitably causes incremental system complexity (4, 12–16). In this sense, various strategies using the conventional complementary metal-oxide semiconductor (CMOS) devices have been proposed to relieve system complexity upon the densification (16–21) including a multivariable proportional integration differential (PID)–based control system (22–24) and a parallel-to-serial converter (25–28), but they have a fundamental limitations of the serial processing (29, 30). Therefore, a multiplexing unit capable of processing multiple sensor inputs in parallel has emerged as an alternative to overcome this limitation (27, 31–33). While a majority of conventional transistors lack the ability to process multiple inputs in parallel, synaptic transistors with polymeric ion gel dielectrics can be excellent tools for implementing the function of a multiplexing unit. This is due to the characteristics of the synaptic transistor, in which the current density of the semiconductor channel is determined by the concurrent sum of the electric fields applied to the polymeric ion gel dielectric (34–38). On the basis of the working mechanism of the ion gel synaptic transistor, parallel signal processing can be achieved by simply designing multiple gate electrodes on the ion gel dielectric.

The capability of parallel signal processing in a synaptic transistor is essential for realizing a closed-loop control system. This system is

driven by reducing the difference between the target and set values of the object. Unlike an open-loop control system, which operates by simply setting an input, a closed-loop control system can cope with changes in external conditions and can accurately reach the target value compared to its counterpart (39). However, closed-loop control systems presuppose the ability to simultaneously receive external factors along with signals for the complementary response for correction (40–46). That is, multiple signals should be processed parallelly to contribute to the output. Traditional CMOS technology, as well acknowledged, is capable of such parallel signal processing. However, it posits the incorporation of the analog-to-digital converter, digital-to-analog converter, and CMOS signal processor to the system. Those additional components for the parallel processing inevitably accompany the integration of numerous transistors, which can cause high energy consumption and the von Neumann bottleneck as the system complexity increases with increasing amounts of inputs. On the contrary, a single synaptic transistor-based multiplexer can process multiple signals simultaneously without extra computational processes. Therefore, the replacement of circuit components with a single synaptic device can greatly reduce the circuit complexity. Therefore, by designing a closed-loop control system with the multiplexing characteristics of synaptic transistors, environment-resistive control can be realized.

In this study, a closed-loop multi-input control system was realized via introducing an artificial synaptic multiplexing unit capable of simultaneously processing various sensory inputs. Three components, namely, the sensor, actuator, and multiplexing unit, were fabricated as the form of fiber to comprise a closed-loop control system with compact and versatile applicability for the flexible robotics and wearable electronics. A fiber-type sensor that can detect the bending motion of an actuator was developed. A soft actuator with a wide bending range and a small form factor was fabricated using a shape memory alloy (SMA) fiber. A fiber-type synaptic transistor with a poly(3-hexylthiophene) (P3HT) semiconductor channel and an ion gel gate dielectric was used as the multiplexing unit. The saturation current of the synaptic transistor was regulated by the feedback signal from the sensor directly attached on top of the actuator as well as the environmental input signal, which corrects the potentiation of the multiplexing unit. On the basis of the parallel signal processing capability of the artificial synaptic multiplexing unit, a

Copyright © 2022
The Authors, some
rights reserved;
exclusive licensee
American Association
for the Advancement
of Science. No claim to
original U.S. Government
Works. Distributed
under a Creative
Commons Attribution
NonCommercial
License 4.0 (CC BY-NC).

¹Department of Chemical and Biomolecular Engineering, Yonsei University, Seoul 120-749, Republic of Korea. ²School of Electrical and Electronic Engineering, Yonsei University, Seoul 03722, Republic of Korea. ³Department of Mechanical Science and Engineering, University of Illinois at Urbana-Champaign, Urbana, IL 61801, USA. ⁴SKKU Advanced Institute of Nanotechnology (SAINT), Sungkyunkwan University, Suwon 16419, Republic of Korea. ⁵Department of Chemical Engineering, Hanyang University, Seoul 04763, Republic of Korea.

*Corresponding author. Email: jhcho94@yonsei.ac.kr

†These authors contributed equally to this work.

closed-loop control system that regulates the bending motion of a soft actuator under environmental stress was successfully demonstrated.

RESULTS

Artificial synaptic multiplexing unit–based multi-input control system

Figure 1A shows the proposed multi-input control system. By simultaneously receiving information about the actuator and environmental variables such as strain, humidity, and temperature, environment-resistive regulation of the actuator with low system complexity can be achieved. Figure 1B shows a flow diagram of the artificial synaptic multiplexing unit–based multi-input closed-loop control system. In the artificial synaptic multiplexing unit, an environmental signal that can be defined as the change in ambient conditions, such as temperature, humidity, and pressure changes, and various feedback signals caused by physical changes of an actuator enter in parallel with a control input spike. The signals are then transmitted to the actuator after being integrated to adjust the physical state of the actuator. Feedback signals reflecting the updated physical value of the actuator are then delivered to the artificial synaptic multiplexing unit again for subsequent signal integration. A clear representation of the feedback signal transmission within a closed loop is the overactuation protection under environmental stress. A general scheme for controlling a multivariable system involving environmental constraints such as temperature, moisture, pressure, and strain conditions compels the use of incremental addition of PID controllers in conventional von Neumann systems. By demonstrating the environment-resistive

actuation procedure, the feasibility for the successful completion of invulnerable feedback loop via the artificial synaptic multiplexing unit can be corroborated. Figure 1C shows a schematic diagram of a closed-loop control system that has an overactuation protection function as well as environment-resistive characteristics enabled by the artificial synaptic multiplexing unit. The overactuation-protective environment-resistive closed-loop control system has three main components, namely, an artificial synaptic multiplexing unit, an actuator, and a sensor. Each component was designed in the form of fibers, as it is advantageous for large deformations while having a small form factor. The artificial synaptic multiplexing unit receives multiple input signals and delivers one output signal to the actuator. When a signal (V_{input1}) is delivered to the fiber actuator, the fiber contracts, causing bending deformation of the polydimethylsiloxane (PDMS) matrix. The change in the electrical resistance of the sensor due to the physical deformation of the actuator was then applied to the comparator as a voltage spike. Here, a comparator compares the input voltage spike from the sensor to the reference value to determine whether a voltage spike that attenuates the actuation is required to be applied to the artificial synaptic multiplexing unit. If the input signal is higher than the reference value, an indication of overactuation, the comparator transmits a depression feedback signal (V_{input2}) to the artificial synaptic multiplexing unit. As a result of the regulatory feedback process, the bending angle (BA) of the actuator of the closed-loop control system operates securely without inordinate actuation. Furthermore, actuation can be controlled more precisely by adjusting the error caused by ambient temperature. High temperature causes heat to be stored in the PDMS matrix, delaying the

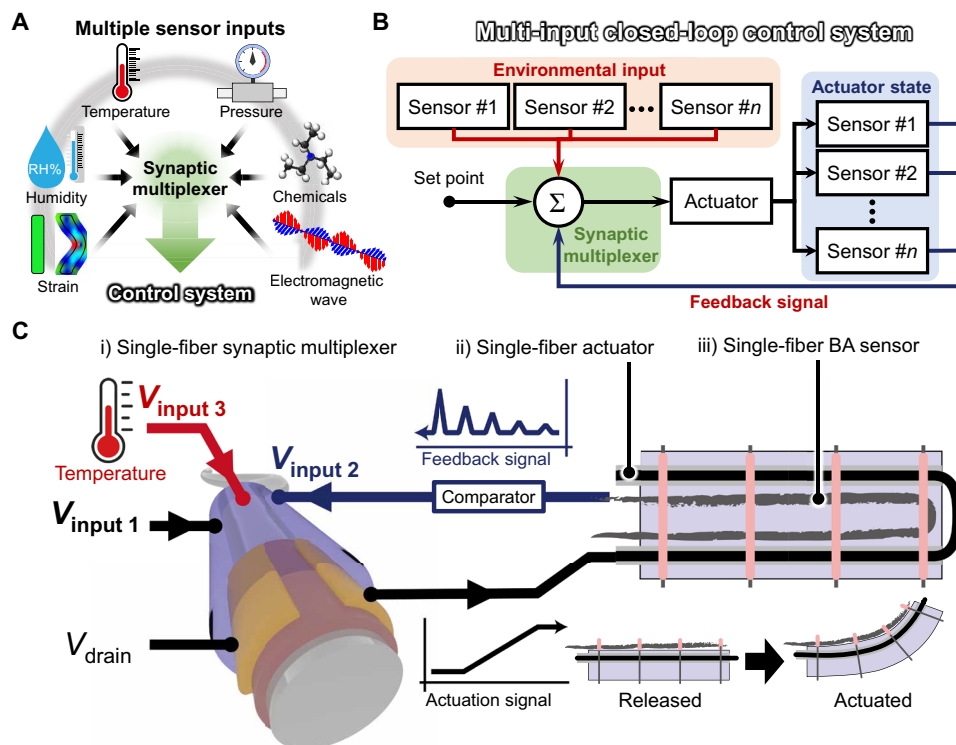


Fig. 1. Logic diagram of the synaptic control system. (A) Illustration of the multi-input control system using an artificial synaptic multiplexing unit. (B) Flow diagram of the multi-input closed-loop control system comprising an artificial synaptic multiplexing unit, an actuator, and multiple sensors. (C) Schematic diagram of the closed-loop control system using a single-fiber artificial synaptic multiplexing unit, a single-fiber actuator, a single-fiber bending angle (BA) sensor, and an environmental signal input circuit.

cooling of the SMA fiber. To minimize the error of control caused by such an unavoidable environmental stressor, the environment-resistive characteristic of the artificial synaptic multiplexer was determined by connecting it with the environmental signal input subcircuit. To this end, as shown in Fig. 1C, an environmental signal input subcircuit that generates a depression signal (V_{input3}) according to the ambient temperature outside the system was fabricated.

Characterization of fiber-type BA sensor and soft actuator

To monitor the movement of the soft actuator, a BA sensor was designed in the form of a fiber (Fig. 2A). The BA sensor comprised chemical and friction-resistant poly(vinylidene fluoride-co-hexafluoropropylene) (PVDF-HFP) nonwoven nanofibers and $Ti_3C_2T_x$ MXene with high electrical conductivity. Specifically, the PVDF-HFP acetone solution was blow-spun. MXene solution, synthesized using a previously reported method (fig. S1), was then spray-coated thereon (fig. S2). After drying, the conductive nonwoven fabric film was rolled up to form a 30-cm-long single strand and cut to the desired length (Fig. 2B and fig. S3). The resulting BA sensor consisted of numerous strands of nanofibers entangled with each other, as shown in Fig. 2C. Figure 2D shows the energy-dispersive x-ray spectroscopy (EDS) images of the fiber BA sensor. Fluorine abundantly present in PVDF-HFP and titanium of MXene were

evenly distributed, indicating that the MXene was uniformly coated on the fiber strand. Figure 2E shows the electrical resistance change of the BA sensor as a function of BA, defined as the angular displacement of the free end of the fixed end as its central axis. The BA sensor had good sensitivity over a wide range of BA up to 90°: its electrical resistance decreased with a sensitivity of 5.08 gigohms/° and 2.80 megohms/° in the low ($\theta < 43^\circ$) and high ($\theta > 43^\circ$) BA region, respectively. This decrease in electrical resistance may be attributed to bending due to the structural properties of the BA sensor. The electrical resistance decreased because the MXene flakes that were electrically isolated on top of the nonwoven PVDF-HFP nanofiber matrix that can be deformed by the external force were connected to the adjacent MXene flakes by bending (47–49). Figure 2F shows the real-time resistance change of the BA sensor for various BAs. The electrical resistance decreased by BA returned to the original resistance level when bending was released, and the resistance drop was more drastic as BA increased. The BA sensor also exhibited outstanding electrical stability, as shown in Fig. 2G. During the cyclic bending test with a BA of 60° up to 500 bending cycles, the electrical resistance in the bent as well as released states remained unchanged. Furthermore, response times of 210 and 500 ms were measured for bending and releasing at 10°, respectively, as shown in Fig. 2H.

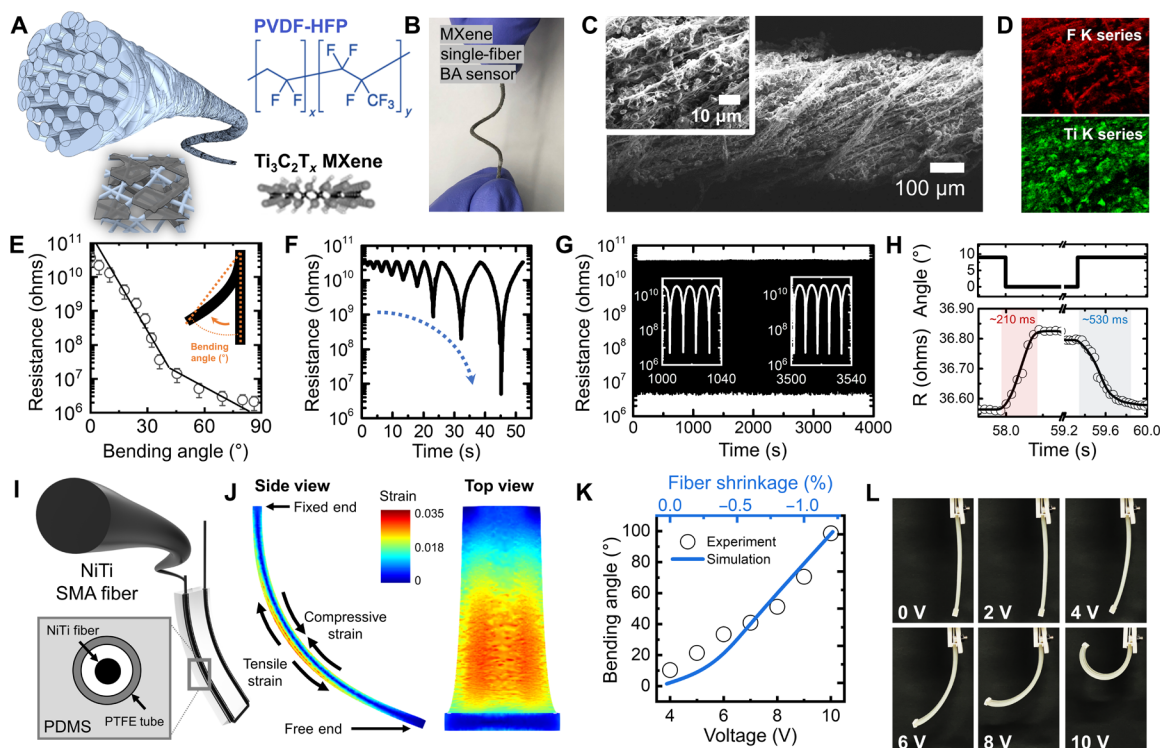


Fig. 2. Characteristics of single-fiber BA sensor and soft actuator. (A) Three-dimensional illustration of the BA sensor and the structural formula of poly(vinylidene fluoride-co-hexafluoropropylene) (PVDF-HFP) and MXene. (B) Photograph of the BA sensor. (C) Scanning electron microscopy image of the surface of the BA sensor. (D) Energy-dispersive x-ray spectroscopy mapping images showing the distribution of chemical elements in the MXene-coated BA sensor (F and Ti). (E) BA versus electrical resistance characteristics of the BA sensor. Inset shows the definition of BA. (F) Real-time dynamics of the BA sensor with the various BAs (4.5°, 7°, 10°, 12°, 14°, 16°, 24°, 32°, and 65°). (G) BA sensor stability test using a BA of 65° up to 500 cycles. (H) Minimum BA and response characteristics of the sensor. The top graph shows the signal applied to the bending machine, and the bottom graph shows the real-time signal response of the BA sensor. (I) Three-dimensional illustration of the soft actuator using NiTi shape memory alloy fiber and a 2D cross-sectional illustration of the actuator. PDMS, polydimethylsiloxane; PTFE, polytetrafluoroethylene. (J) Side and top views of the distribution of the strain applied to the actuator based on the simulated results. (K) Soft actuator BA results of the experiment and simulation depending on the voltage and fiber shrinkage, respectively. (L) Photographs of the soft actuator according to the applied voltage.

The actuator was fabricated by passing a NiTi SMA fiber (diameter = 500 μm) through a polytetrafluoroethylene (PTFE) tube thinly embedded in a PDMS matrix, as shown in Fig. 2I. Upon the application of electricity, the NiTi SMA in the martensite phase transformed to the memorized austenite phase by joule heating, and the accompanying structural deformation shortened the length of the fiber (fig. S4). The relaxation action of NiTi SMA is performed by cooling. NiTi SMA in austenite turns into relaxed martensite when cooled to its transition temperature. The shrinkage of the NiTi fibers induced compressive strain on the side where the fiber was shallowly embedded and tensile strain on the opposite side, leading to the bending actuation of the PDMS matrix. Figure 2J shows the strain distribution of the actuator obtained from the bending simulation result of the three-dimensional (3D)-modeled actuator with the same pressure allocation as that of the NiTi fiber-embedded PDMS actuator. The simulated strain distribution was consistent with the theoretically predicted strain distribution, confirming the bending mechanism described above. Figure 2K shows a good correlation between the applied voltage-BA relation and that of fiber shrinkage-BA analyzed from the bending simulation, which further provides evidence of bending by fiber shrinkage. Figure 2L shows the photographic images of the actuator according to the applied voltages. No prominent actuator bending was observed until 4 V. However, the actuator bent substantially when the voltage exceeded 6 V, implying the presence of a phase transformation.

Electrical characterization of ion gel-based artificial synaptic multiplexing unit

To properly process multiple signals (a feedback signal and environmental signals) and transmit them to the actuator, it is important to

understand the characteristics of the multigate artificial synaptic multiplexing unit. Figure 3A shows a schematic of a single-gate synaptic transistor on a nylon fiber. We chose nylon fiber because of its various advantages such as high chemical resistivity, tensile strength, and compressive strength, which are suitable traits for realizing flexible robotics and wearable electronics in future. The nylon fiber substrate was deposited with a P3HT semiconductor channel, gold electrodes, and an ion gel dielectric layer (optical microscope image in fig. S5). To estimate the synaptic performance of the fiber-shaped single-gate synaptic transistor, various electrical measurements were performed. First, the transfer curve and excitatory postsynaptic current (PSC)/inhibitory PSC showed a large hysteresis and long retention time, respectively (figs. S6 and S7). In addition, long-term potentiation/depression (LTP/D) characteristics were evaluated through current-voltage measurements, as shown in Fig. 3B. As an input spike (V_{G1}), various amplitudes of 50 potentiation spikes ($V_{G1} = -2\text{ V}, -2.5\text{ V}, -3\text{ V}$) followed by 50 depression spikes ($V_{G1} = +2\text{ V}$) were applied at a drain voltage of 0.5 V, as shown in the top panel of Fig. 3B. The PSC increased and decreased consistently during the continuous potentiation spikes and depression spikes, respectively, and the change in PSC was larger as the amplitude of the spikes was greater (bottom panel). PSC dependency on the amplitude of the depression spike was also measured by applying 50 potentiation spikes ($V_{G1} = -3\text{ V}$) followed by 50 depression spikes ($V_{G1} = +2\text{ V}, +2.5\text{ V}, +3\text{ V}$), showing a consistent decrease in saturation current as the depression voltage increased (fig. S8). Moreover, LTP/D characteristics of the artificial synaptic multiplexing unit were observable until 3 kHz (fig. S9).

In the case of a dual-gate artificial synaptic multiplexing unit, two different input spikes were simultaneously applied to each gate

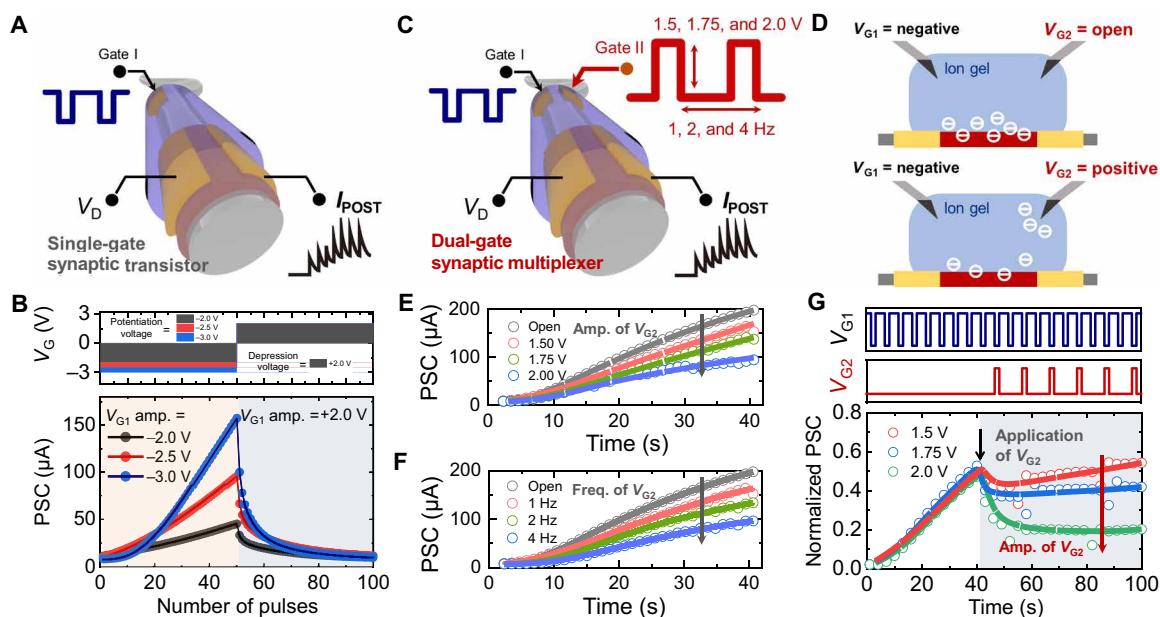


Fig. 3. Operation characteristics and mechanism of the artificial synaptic multiplexing unit. (A) Schematic diagram of the single-gate synaptic transistor. (B) Long-term potentiation and long-term depression characteristics of the single-gate synaptic transistor at potentiation and depression voltages of -2 , -2.5 , -3 , and 2 V , respectively. (C) Schematic diagram of the dual-gate artificial synaptic multiplexing unit. Negative and positive voltage spikes are applied to gate 1 and gate 2, respectively. (D) Schematic illustration of the multi-gate artificial synaptic multiplexing unit operation mechanism. Postsynaptic current (PSC) characteristics of a dual-gate artificial synaptic multiplexing unit when various amplitudes (E) and frequencies (F) of depression voltage spikes are applied to gate 2 (gate 1 = -3 V). (G) Real-time demonstration of the characteristics of an artificial synaptic multiplexing unit when depression spikes and potentiation spikes are simultaneously applied.

for signal multiplexing, as depicted in Fig. 3C. Specifically, negative (V_{G1}) and positive spikes (V_{G2}) were applied to gates I and II, respectively. When gate II is open and only negative V_{G1} is applied, it follows the working mechanism of the single-gate synaptic transistor: Under the application of a negative voltage spike, mobile anions (PF_6^-) that retracted from the gate electrode by electrical repulsion in the ion gel can easily penetrate the free volume of the semiconducting P3HT layer and temporarily dope the semiconductor channel that increases the PSC, as illustrated in the top panel of Fig. 3D. In contrast, some anions are extracted from the free volume by the electrical attraction of gate II when positive V_{G2} is applied. Therefore, the penetration of the anions into the P3HT layer is disturbed and the PSC increase is inhibited. This presumption of the effect of positive V_{G2} on PSC is shown in Fig. 3E. To confirm the contribution of V_{G2} to PSC, -3 V, which caused the greatest increase in PSC (Fig. 3B), was selected as the amplitude of V_{G1} . The amplitude of V_{G2} was given as 1.50, 1.75, and 2.00 V as well as an open state, and the frequencies of V_{G1} and V_{G2} were all 1 Hz. As the amplitude of V_{G2} increased, the PSC showed a tendency to decrease. The decrease in PSC was also dependent on the frequency of V_{G2} , as shown in Fig. 3F; the higher the frequency, the greater the decrease in the PSC. Figure 3G shows real-time normalized PSC measurements according to V_{G1} and V_{G2} inputs. A negative V_{G1} spike of -3 V, 2.5 Hz was applied throughout the test. Up to $t = 40$ s, only a positive V_{G1} spike was applied to increase the PSC level. From $t = 40$ s, negative V_{G2} spikes of 1 Hz were applied with amplitudes of 1.5, 1.75, and 2.0 V. The resulting increasing PSC was partly suppressed while maintaining an increasing trend under 1.5 V of V_{G2} , and it eventually decreased when the applied V_{G2} increased to 2.0 V. The feasibility

of artificial synaptic multiplexing behavior by three or more gates is shown in fig. S10. When four potentiation spikes were given ($V_{G0} = -3$ V, $V_{G1} = -1.5$ V, $V_{G2} = -1.5$ V, and $V_{G3} = -1.5$ V), the saturation current of PSC was measured to 197 μA . However, when one potentiation and three depression spikes were given ($V_{G0} = -3$ V, $V_{G1} = 1.5$ V, $V_{G2} = 1.5$ V, and $V_{G3} = 1.5$ V), the saturation current of PSC decreased to 95 μA . As the number of gates applying potentiation spikes increased, the saturation current level of the PSC increased. This result shows that the artificial synaptic multiplexing unit can successfully process the signal even when several inputs are provided.

Demonstrations of multi-input control system

Last, an artificial synaptic multiplexing unit-based multi-input control system was fabricated by incorporating the functions of an artificial synaptic multiplexing unit, actuator, and sensor. Figure 4 (A and B) shows a closed-loop feedback circuit diagram of the environment-resistive overactuation protection system and its signal flow at each phase, respectively. Overall, the system comprises three subcircuits: (i) an artificial synaptic multiplexing unit circuit that integrates signals and delivers it to the actuator, (ii) a feedback circuit in which the sensor detects the overactuation of the actuator and provides a depression signal to the artificial synaptic multiplexing unit, and (iii) an environmental signal input circuit that provides a depression signal in terms of external temperature variance to the artificial synaptic multiplexing unit. The combination of these circuits enables the realization of a feedback system based on the artificial synaptic multiplexing unit. First, an artificial synaptic multiplexing unit converts the negative voltage spike applied to its gate (for BA control) into a PSC, followed by an RC delay for signal amplification and

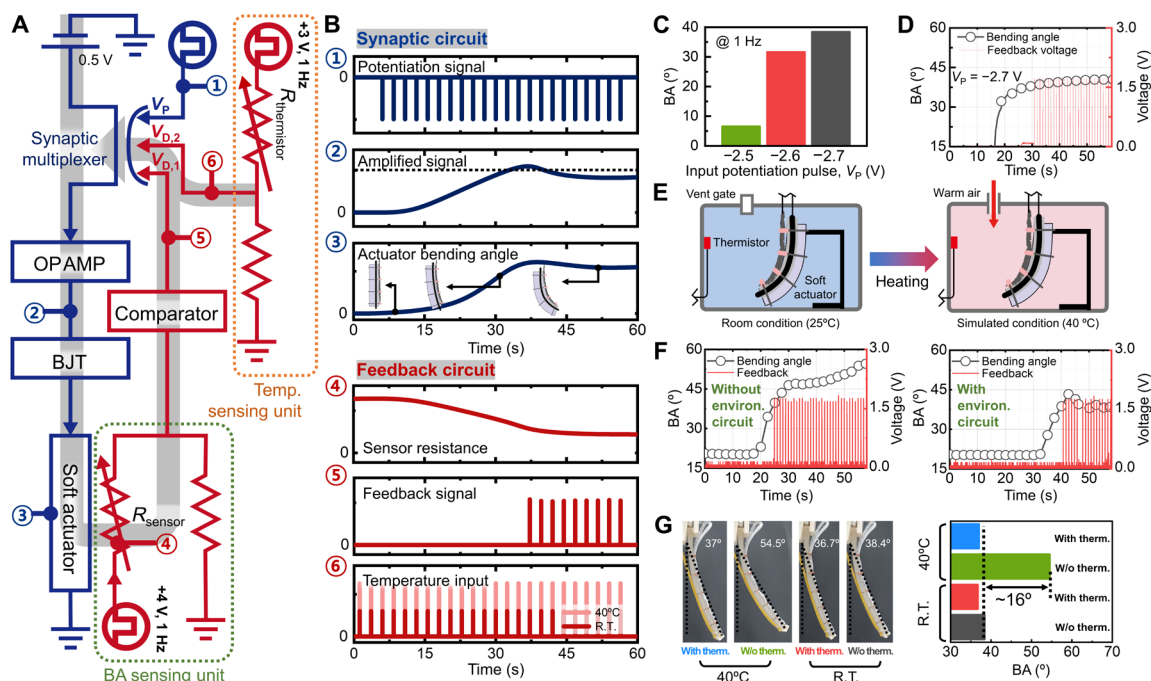


Fig. 4. Operation of a closed-loop control system based on artificial synaptic multiplexing unit. (A) Circuit diagram of a closed-loop control system. (B) Conceptual graphs of signals at designated points. (C) BA of the soft actuator depending on the amplitude of the input potentiation voltage spike. (D) BA and feedback voltage signal as functions of time. (E) Experimental scheme simulating the warm ambient temperature condition. (F) BA and feedback voltage signal as a function of time at 40°C without (left) and with (right) environmental signal input circuit, respectively. (G) Photographic images of bending of the soft actuator according to ambient temperature [40°C and room temperature (25°C)] and the presence of environmental signal input circuit (left) and BA of the soft actuator in each condition (right).

filtering (Fig. 4, A and B ① and ②, and fig. S11A). Subsequently, the signal, power-enhanced by the bipolar junction transistor, enters the soft actuator to gradually bend it (Fig. 4, A and B ③, and fig. S11B). The bending of the soft actuator causes a decrease in the electrical resistance of the fiber BA sensor mounted on the actuator (Fig. 4, A and B ④, and fig. S11C). The decrease in the sensor resistance results in an increase in the amplitude of the positive voltage spikes generated by the voltage divider. After passing through the voltage divider, the voltage spike is applied to the comparator, which compares the value of the applied voltage spike with a reference spike. When the level of the applied voltage spike exceeds the reference threshold, which indicates overactuation of the soft actuator, the depression signal is induced from the voltage divider and is delivered to the artificial synaptic multiplexing unit, ensuring that the soft actuator securely remains within a desirable BA range (Fig. 4B ⑤).

To achieve environment resistance, an environmental sensing unit was additionally designed to minimize the unwanted bending due to the external temperature. Although PDMS contributes to the soft nature of the actuator, it is prone to accumulate heat from the ambient environment and deform itself, causing an error in the BA. Therefore, depressing signals that minimize the heat-induced bending error should be presented in addition to the overactuation protective feedback system. This bending correction is governed by the generation of a depression signal from a thermistor and voltage divider (Fig. 4A, top right). The higher the temperature, the lower the resistance of the thermistor and the higher the positive voltage spikes applied to the artificial synaptic multiplexing unit (Fig. 4B ⑥).

The overactuation protection of the soft actuator was demonstrated on the basis of the concept of the depression signals described above. First, the amplitudes of the control input potentiation spikes (V_P) were taken as -2.5 , -2.6 , and -2.7 V with a frequency of 1 Hz to investigate the change in BA according to the input spike. As the amplitude of V_P increased, the saturation current of the artificial synaptic multiplexer and BA increased by $135 \mu\text{A}$ and 31° , respectively, as shown in Fig. 4C and fig. S12. As shown in Fig. 4D and movie S1, when the soft actuator reached the overactuation bending point (BA = 39°) at 30 s under the V_P of -2.7 V, $+1.9$ V of depression voltage spike ($V_{D,1}$) was applied to the artificial synaptic multiplexer by a comparator to depress the overactuation of the soft actuator. Conversely, in case of -2.5 and -2.6 V, the overactuation protecting depression voltage spikes were not applied to the artificial synaptic multiplexer unit owing to the low BA, as shown in fig. S13. Figure 4E shows the environment-resistive control of the soft actuator enabled by overactuation protection. To create a warm environment (40°C), a chamber containing a soft actuator and thermistor was heated by blowing warm air (70°C) through the vent gate. The effect of the increased temperature on the bending error is shown in the left panel of Fig. 4F (see movie S2). At 40°C and a V_P of -2.7 V, the heat accumulation caused overactuation of the soft actuator and showed a noticeable error compared to the room temperature BA condition, regardless of the depression signal ($V_{D,1}$) (fig. S14). However, when the environmental signal input circuit was applied to the artificial synaptic multiplexer, the BA of the soft actuator was controlled more precisely, thereby maintaining a BA similar to that at room temperature (Fig. 4F, right, and movie S3). Figure 4G shows photographic images of bending of the soft actuator according to the ambient temperature (40°C and room temperature) and the presence of an environmental signal input circuit. In the absence of the environmental signal input signal, the temperature increased from room temperature

to 40°C , resulting in a notable increase in BA. In contrast, when the circuit was introduced, the environmental signal input voltage spike ($V_{D,2}$) effectively reduced the BA by 17.5° to reach a BA similar to that at room temperature. The overactuation function showed consistent behavior regardless of the temperature change even at 35°C , as shown in fig. S15. This BA behavior is well correlated with the PSC at the output of the artificial synaptic multiplexing unit, as shown in fig. S14. At an ambient temperature of 40°C without an environmental signal input circuit, the PSC reached the overactuation protection level much faster than the other cases, whereas the other three conditions exhibited a PSC behavior similar to that at room temperature conditions. These results confirm that our artificial synaptic multiplexing unit-based multi-input control system can implement environment-resistive physical control of the actuator via a simple synaptic feedback system.

DISCUSSION

The synaptic transistor-based multiplexer capable of simultaneous parallel processing of multiple input signals is proposed, with which a closed-loop multi-input control system was realized. Using ion gel as the dielectric layer of the artificial synaptic multiplexer, multigating was performed for the processing of a parallel input. To demonstrate feedback signal transmission based on signal multiplexing, we built an environment-resistive control system that can maintain the bending of the actuator within a certain range regardless of different environmental stressing, by integrating the functions of the ion gel-based artificial synaptic multiplexer, actuator, BA sensor, and thermistors.

The core idea behind the proposed artificial synaptic multiplexer is the use of the ion-based electrochemical operating mechanism. Considering that the field of electrochemical transistors has been under rigorous investigations and optimizations in various perspectives including semiconductors, dielectrics, and encapsulations, there is plenty of room for advancements in terms of operation speed and miniaturizations of the synaptic multiplexer. The suggested ion gel-based artificial synaptic multiplexing control of the multi-input control system sets the basis for a new field of synaptic functionalities, which demonstrates the immense potential for applications in parallel processing requiring industries and AI.

MATERIALS AND METHODS

Device fabrication

BA sensor

Eleven weight % PVDF-HFP (Sigma-Aldrich, $M_w = 400,000$) solution was prepared by dissolving 5.5 g of PVDF-HFP pellets (44.5 g) in acetone. The solution was stirred for 3 hours at room temperature (25°C). After the PVDF-HFP pellets were completely dissolved, 5 ml of PVDF-HFP solution was poured into the reservoir of an airbrush with a nozzle size of 0.2 mm (FD-116A, Falcon). The airbrush was connected to an air compressor with a maximum pressure of 8.27 bar (ULTRA 340, AirFactory). The aluminum foil collector was placed at a 70° angle to the ground, and the airbrush was triggered with 6.21 bar pressure from a distance of 60 cm to fabricate the PVDF-HFP nanofiber mat. A 5 mg/ml concentration of $\text{Ti}_3\text{C}_2\text{T}_x$ MXene solution was prepared by etching aluminum in 4 g of Ti_3AlC_2 , MAX powder (99%, 200 mesh, Forsman) using LiF/HCl solution as previously reported (50). MXene solution (8 ml) was spray-coated on top of the

as-prepared blow-spun PVDF-HFP nanofiber mat. The MXene-coated nanofiber mat was rolled in one direction to complete the fabrication of the BA sensor.

Soft actuator

A 100 mm by 20 mm by 3 mm (length by width by height) mold for the PDMS soft body was designed (fig. S16) and prepared using a 3D printer (Prusa Mk 3 s). Two PTFE tubes (diameter = 0.92 mm; Misumi, TUBF26-10) for the NiTi SMA fiber path were passed through the holes of the mold. Subsequently, the uncured PDMS (Sylgard 184) was poured into the mold coupled with the PTFE tube and placed in a vacuum for 30 min to remove air bubbles inside the PDMS. Then, the PDMS was cured at 80°C. The mold was removed, and a NiTi SMA fiber was threaded through the PTFE tube to complete the soft actuator (fig. S17).

Artificial synaptic multiplexing unit

P3HT solution was prepared by dissolving P3HT in chloroform at a concentration of 2 mg/ml. The solution was stirred for 3 hours at 50°C under ambient conditions. The ion gel was prepared by mixing poly(ethylene glycol) diacrylate monomer, 2-hydroxy-2-methylpropiophenone initiator, and 1-butyl-3-methylimidazolium hexafluorophosphate ([BMIM][PF₆]) ionic liquid in a weight ratio of 2:1:22. To form the channel of the artificial synaptic multiplexing unit, P3HT was inkjet-printed on a nylon fiber (diameter = 0.5 mm) and dried overnight in Ar. Cr/Au (3/17 nm) was patterned by thermal evaporation through a shadow mask to form the source, drain, and gate electrodes. Last, the ion gel was drop-casted to cover both the channel and the gate electrodes and subsequently cross-linked by ultraviolet irradiation (100 mW/cm² at 365 nm for 8 s).

Measurements

The surface morphologies of the single-fiber BA sensor were measured by a field emission scanning electron microscope (FE-SEM) (JEOL-7800F) in the secondary electron imaging mode with an accelerating voltage of 10 kV. EDS mapping of the fiber was performed using an Oxford Instruments Nanoanalysis unit attached to the FE-SEM. A bending simulation was performed using the SimScale Multiphysics simulation software with the 3D model used to fabricate the soft actuator mold for accurate simulation. The bending of the soft actuator was video-recorded on its side, and BAs were estimated by analyzing the recorded videos using the ImageJ PhotoBend plugin (51). A warm condition of 40°C was simulated by blowing hot air into a 50 cm by 50 cm by 70 cm acrylic box. A thermistor (NTSM-7, Boyuan) was attached to the side of the wall, and the temperature measurement unit was placed at the corner of the acrylic box. The electrical properties of the all devices were measured with a Keithley 4200A-SCS and Tektronix DPO3052 unit.

SUPPLEMENTARY MATERIALS

Supplementary material for this article is available at <https://science.org/doi/10.1126/sciadv.abn1838>

REFERENCES AND NOTES

1. A. Haque, A. Milstein, L. Fei-Fei, Illuminating the dark spaces of healthcare with ambient intelligence. *Nature* **585**, 193–202 (2020).
2. Y. LeCun, Y. Bengio, G. Hinton, Deep learning. *Nature* **521**, 436–444 (2015).
3. A. Billard, D. Kragic, Trends and challenges in robot manipulation. *Science* **364**, eaat8414 (2019).
4. F. Zhou, Y. Chai, Near-sensor and in-sensor computing. *Nat. Electron.* **3**, 664–671 (2020).
5. J. Schmidt, M. R. G. Marques, S. Botti, M. A. L. Marques, Recent advances and applications of machine learning in solid-state materials science. *Npj Comput. Mater.* **5**, 83 (2019).
6. Y. Shen, F. E. Shamout, J. R. Oliver, J. Witowski, K. Kannan, J. Park, N. Wu, C. Huddleston, S. Wolfson, A. Millet, R. Ehrenpreis, D. Awal, C. Tyma, N. Samreen, Y. Gao, C. Chhor, S. Gandhi, C. Lee, S. Kumari-Subaiya, C. Leonard, R. Mohammed, C. Moczulski, J. Altabet, J. Babb, A. Lewin, B. Reig, L. Moy, L. Heacock, K. J. Geras, Artificial intelligence system reduces false-positive findings in the interpretation of breast ultrasound exams. *Nat. Commun.* **12**, 5645 (2021).
7. E. L. Aiken, A. T. Nguyen, C. Viboud, M. Santillana, Toward the use of neural networks for influenza prediction at multiple spatial resolutions. *Sci. Adv.* **7**, eabb1237 (2021).
8. J. Y. Park, C. A. Stock, J. P. Dunne, X. S. Yang, A. Rosati, Seasonal to multiannual marine ecosystem prediction with a global Earth system model. *Science* **365**, 284–288 (2019).
9. A. F. Zahrt, J. J. Henle, B. T. Rose, Y. Wang, W. T. Darrow, S. E. Denmark, Prediction of higher-selectivity catalysts by computer-driven workflow and machine learning. *Science* **363**, 247 (2019).
10. G. Ganesh, K. Nakamura, S. Saetia, A. M. Tobar, E. Yoshida, H. Ando, N. Yoshimura, Y. Koike, Utilizing sensory prediction errors for movement intention decoding: A new methodology. *Sci. Adv.* **4**, eaaq0183 (2018).
11. J. Briscoe, O. Marín, Looking at neurodevelopment through a big data lens. *Science* **369**, eaaz8627 (2020).
12. V. Beiu, J. G. Taylor, On the circuit complexity of sigmoid feedforward neural networks. *Neural Netw.* **9**, 1155–1171 (1996).
13. I. Parberry, M. R. Garey, A. Meyer, *Circuit Complexity and Neural Networks* (MIT Press, 1994).
14. S. Swanson, A. M. Caulfield, Refactor, reduce, recycle: Restructuring the I/O stack for the future of storage. *Computer* **46**, 52–59 (2013).
15. A. Ailamaki, Databases and hardware: The beginning and sequel of a beautiful friendship. *Proc. VLDB Endow.* **8**, 2058–2061 (2015).
16. P. A. Merolla, J. V. Arthur, R. Alvarez-Icaza, A. S. Cassidy, J. Sawada, F. Akopyan, B. L. Jackson, N. Imam, C. Guo, Y. Nakamura, B. Brezzo, I. Vo, S. K. Esser, R. Appuswamy, B. Taba, A. Amir, M. D. Flickner, W. P. Risk, R. Manohar, D. S. Modha, A million spiking-neuron integrated circuit with a scalable communication network and interface. *Science* **345**, 668–673 (2014).
17. Y. Suhail, K. G. Oweiss, A reduced complexity integer lifting wavelet based module for real-time processing in implantable neural interface devices, in *The 26th Annual International Conference of the IEEE Engineering in Medicine and Biology Society (IEEE, 2004)*, vol. 2, pp. 4552–4555.
18. R. Canal, A. González, Reducing the complexity of the issue logic, in *Proceedings of the 15th International Conference on Supercomputing (Association for Computing Machinery, 2001)*, pp. 312–320.
19. R. S. Saxena, R. K. Bhan, A. Aggrawal, Reducing readout complexity of large resistive sensor arrays. *IEEE Sens. J.* **8**, 1862–1863 (2008).
20. P. Narayanan, G. W. Burr, R. M. Shelby, S. Ambrogio, H. Tsai, S. L. Lewis, K. Hosokawa, Neuromorphic devices and architectures for next-generation cognitive computing, in *2017 IEEE International Symposium on Circuits and Systems (ISCAS)*, (IEEE, 2017), pp. 1–4.
21. S. Dutta, A. Khanna, A. S. Assoa, H. Paik, D. G. Schlom, Z. Toroczka, A. Raychowdhury, S. Datta, An Ising Hamiltonian solver based on coupled stochastic phase-transition nano-oscillators. *Nat. Electron.* **4**, 502–512 (2021).
22. F. Merrikh-Bayat, Multivariable proportional-integral-derivative controller tuning via linear matrix inequalities based on minimizing the nonconvexity of linearized bilinear matrix inequalities. *J. Dyn. Syst. Meas. Control* **140**, 111012 (2018).
23. L. D. Coelho, M. W. Pessôa, A tuning strategy for multivariable PI and PID controllers using differential evolution combined with chaotic Zaslavskii map. *Expert Syst. Appl.* **38**, 13694–13701 (2011).
24. F. Zheng, Q. G. Wang, T. H. Lee, On the design of multivariable PID controllers via LMI approach. *Automatica* **38**, 517–526 (2002).
25. A. Parashar, P. Anand, A. Abraham, Computer vision, pattern recognition, image processing, and graphics, in *7th National Conference, NCVPRIP2019*, Hubballi, India, December 22–24, 2019; Revised selected papers (Springer, Singapore, 2020), pp. 250–260.
26. A. Hasan, K. Qureshi, in *2018 International Conference on Applied and Engineering Mathematics (ICAEM)*, Taxila, Pakistan (IEEE, 2018), pp. 109–114.
27. Y. Gao, D. T. Nguyen, T. Yeo, S. B. Lim, W. X. Tan, L. E. Madden, L. Jin, J. Y. K. Long, F. A. B. Aloweni, Y. J. A. Liew, M. L. L. Tan, S. Y. Ang, S. D. Maniya, I. Abdelwahab, K. P. Loh, C.-H. Chen, D. L. Becker, D. Leavesley, J. S. Ho, C. T. Lim, A flexible multiplexed immunosensor for point-of-care in situ wound monitoring. *Sci. Adv.* **7**, eabg9614 (2021).
28. N. Bozinovic, Y. Yue, Y. Ren, M. Tur, P. Kristensen, H. Huang, A. E. Willner, S. Ramachandran, Terabit-scale orbital angular momentum mode division multiplexing in fibers. *Science* **340**, 1545–1548 (2013).
29. Big data needs a hardware revolution. *Nature* **554**, 145–146 (2018).
30. K. Roy, A. Jaiswal, P. Panda, Towards spike-based machine intelligence with neuromorphic computing. *Nature* **575**, 607–617 (2019).
31. Z. Liu, J. Tang, B. Gao, X. Li, P. Yao, Y. Lin, D. Liu, B. Hong, H. Qian, H. Wu, Multichannel parallel processing of neural signals in memristor arrays. *Sci. Adv.* **6**, eabc4797 (2020).
32. H. M. Fahad, H. Shiraki, M. Amani, C. Zhang, V. S. Hebbbar, W. Gao, H. Ota, M. Hettick, D. Kiriya, Y.-Z. Chen, Y.-L. Chueh, A. Javey, Room temperature multiplexed gas sensing using chemical-sensitive 3.5-nm-thin silicon transistors. *Sci. Adv.* **3**, e1602557 (2017).

33. B. W. An, S. Heo, S. Ji, F. Bien, J. U. Park, Transparent and flexible fingerprint sensor array with multiplexed detection of tactile pressure and skin temperature. *Nat. Commun.* **9**, 2458 (2018).
34. Y. Choi, S. Oh, C. Qian, J. H. Park, J. H. Cho, Vertical organic synapse expandable to 3D crossbar array. *Nat. Commun.* **11**, 4595 (2020).
35. F. Molina-Lopez, T. Z. Gao, U. Kraft, C. Zhu, T. Öhlund, R. Pfattner, V. R. Feig, Y. Kim, S. Wang, Y. Yun, Z. Bao, Inkjet-printed stretchable and low voltage synaptic transistor array. *Nat. Commun.* **10**, 2676 (2019).
36. J. H. Cho, J. Lee, Y. He, B. S. Kim, T. P. Lodge, C. D. Frisbie, High-capacitance ion gel gate dielectrics with faster polarization response times for organic thin film transistors. *Adv. Mater.* **20**, 686–690 (2008).
37. J. Lenz, F. del Giudice, F. R. Geisenhof, F. Winterer, R. T. Weitz, Vertical, electrolyte-gated organic transistors show continuous operation in the MA cm⁻² regime and artificial synaptic behaviour. *Nat. Nanotechnol.* **14**, 579–585 (2019).
38. H. Shim, K. Sim, F. Ershad, P. Yang, A. Thukral, Z. Rao, H.-J. Kim, Y. Liu, X. Wang, G. Gu, L. Gao, X. Wang, Y. Chai, C. Yu, Stretchable elastic synaptic transistors for neurologically integrated soft engineering systems. *Sci. Adv.* **5**, eaax4961 (2019).
39. N. Mehrabi, J. McPhee, Chapter four—Model-based control of biomechatronic systems, in *Handbook of Biomechatronics*, J. Segil, Ed. (Academic Press, 2019), pp. 95–126.
40. Y. Lee, S. Park, M. Lee, PID controller tuning to obtain desired closed loop responses for cascade control systems. *Ind. Eng. Chem. Res.* **37**, 1859–1865 (1998).
41. K. Turksay, E. S. Bayrak, L. Quinn, E. Littlejohn, A. Cinar, Multivariable adaptive closed-loop control of an artificial pancreas without meal and activity announcement. *Diabetes Technol. Ther.* **15**, 386–400 (2013).
42. J. P. Lynch, Y. Wang, R. A. Swartz, K. C. Lu, C. H. Loh, Implementation of a closed-loop structural control system using wireless sensor networks. *Struct. Control Health Monit.* **15**, 518–539 (2008).
43. L. Zollo, G. Di Pino, A. L. Ciancio, F. Ranieri, F. Cordella, C. Gentile, E. Noce, R. A. Romeo, A. D. Bellingegni, G. Vadalà, S. Miccinilli, A. Mioli, L. Diaz-Balzani, M. Bravi, K.-P. Hoffmann, A. Schneider, L. Denaro, A. Davalli, E. Gruppioni, R. Sacchetti, S. Castellano, V. D. Lazzaro, S. Sterzi, V. Denaro, E. Guglielmelli, Restoring tactile sensations via neural interfaces for real-time force-and-slippage closed-loop control of bionic hands. *Sci. Robot.* **4**, aau9924 (2019).
44. C. K. Boughton, A. Tripyla, S. Hartnell, A. Daly, D. Herzig, M. E. Wilinska, C. Czerlau, A. Fry, L. Bally, R. Hovorka, Fully automated closed-loop glucose control compared with standard insulin therapy in adults with type 2 diabetes requiring dialysis: An open-label, randomized crossover trial. *Nat. Med.* **27**, 1471–1476 (2021).
45. S. Kenkel, S. Mittal, R. Bhargava, Closed-loop atomic force microscopy-infrared spectroscopic imaging for nanoscale molecular characterization. *Nat. Commun.* **11**, 3225 (2020).
46. B. Shih, D. Shah, J. Li, T. G. Thuruthel, Y.-L. Park, F. Iida, Z. Bao, R. Kramer-Bottiglio, M. T. Tolley, Electronic skins and machine learning for intelligent soft robots. *Sci. Robot.* **5**, aaz9239 (2020).
47. Y. B. Bu, T. Shen, W. Yang, S. Yang, Y. Zhao, H. Liu, Y. Zheng, C. Liu, C. Shen, Ultrasensitive strain sensor based on superhydrophobic microcracked conductive Ti₃C₂T_x MXene/paper for human-motion monitoring and E-skin. *Sci. Bull.* **66**, 1849–1857 (2021).
48. H. Zhang, X. M. Tao, T. X. Yu, S. Y. Wang, Conductive knitted fabric as large-strain gauge under high temperature. *Sens. Actuator A Phys.* **126**, 129–140 (2006).
49. D. H. Du, P. C. Li, J. Y. Ouyang, Graphene coated nonwoven fabrics as wearable sensors. *J. Mater. Chem. C* **4**, 3224–3230 (2016).
50. B. Lyu, Y. Choi, H. Jing, C. Qian, H. Kang, S. Lee, J. H. Cho, 2D MXene–TiO₂ core–shell nanosheets as a data-storage medium in memory devices. *Adv. Mater.* **32**, 1907633 (2020).
51. S. Chizhik, A. Sidelnikov, B. Zakharov, P. Naumov, E. Boldyreva, Quantification of photoinduced bending of dynamic molecular crystals: From macroscopic strain to kinetic constants and activation energies. *Chem. Sci.* **9**, 2319–2335 (2018).

Acknowledgments

Funding: This research was supported by Creative Materials Discovery Program through the National Research Foundation of Korea (NRF) funded by the Ministry of Science and ICT (NRF-2019M3D1A1078299) and the National R&D Program through the NRF funded by the Ministry of Science and ICT (2021M3D1A2049315). **Author contributions:** J.H.C. initiated and supervised all the research. D.H.H. and D.G.R. carried out and designed most of the experimental work and data analysis. Y.J.C. analyzed an artificial synaptic multiplexer. Y.Y.C. assisted in the manuscript writing. S.K. assisted in the conceptualization and validation of research. D.H.K. and S.B.J. assisted in the data analysis. All authors discussed the results and contributed to the writing of the manuscript. **Competing interests:** The authors declare that they have no competing interests. **Data and materials availability:** All data needed to evaluate the conclusions in the paper are present in the paper and/or the Supplementary Materials.

Submitted 10 November 2021

Accepted 6 May 2022

Published 22 June 2022

10.1126/sciadv.abn1838